ACS Partner Journal

CHEMICAL & BIOMEDICAL IMAGING

Open Access



pubs.acs.org/ChemBioImaging

Article

# Determining the Multivalent Effects of D-Peptide-Based Radiotracers

Siqi Zhang,[▽] Xiaona Sun,[▽] Wenhao Liu,[▽] Jiang Wu, Yuxuan Wu, Shuo Jiang, Xingkai Wang, Xin Gao, Quan Zuo, Hailong Zhang, Yingzi Zhang, Feng Wang, Rui Wang,* and Kuan Hu*

Cite This: *Chem. Biomed. Imaging* 2025, 3, 180−190

Read Online

ACCESS | Metrics & More | Article Recommendations | Supporting Information

**ABSTRACT:** Dextrorotary (D) peptides, composed of D-amino acids, are hyper-resistant to proteolytic hydrolysis, making them valuable ligands with excellent *in vivo* stability for radiopharmaceutical development. Multimerization is a well-established strategy for enhancing the *in vivo* performance of L-peptide-based radiopharmaceuticals. However, the effect of multimerization on the *in vivo* fate of D-peptide-based radiopharmaceuticals remains largely unexplored. Here, we synthesized the D-peptide DPA, which targets PD-L1, along with its dimer (DP2) and trimer (DP3). PET/CT imaging and *ex vivo* biodistribution studies were performed to delineate the pharmacokinetics and target interactions of [$^{68}$Ga]DPA, [$^{68}$Ga]DP2, and [$^{68}$Ga]DP3 in both normal and tumor-bearing mice. Our results revealed that tumor uptake and kidney retention increased with higher valency ([$^{68}$Ga]DP3 > [$^{68}$Ga]DP2 > [$^{68}$Ga]DPA). No significant differences were observed in the liver, heart, lung, spleen, intestine, or bone among the three radiotracers. Interestingly, a significant reduction of radioactivity in the bloodstream was detected for the [$^{68}$Ga]DP3-treated group compared to the other two groups. Data analysis revealed that chiral configuration of amino acids and the linking chemistry used in multimerization are the two dominant factors in the *in vivo* fate of D-peptide multimers. These findings indicate that D-peptide multimerization exerts a distinct influence on *in vivo* profiles compared to L-peptide multimerization. This study deepens our understanding of how mirror-imaged peptides/proteins interact with the living systems, paving the way for the development of radiopharmaceuticals that harness D-peptides as targeting moieties.

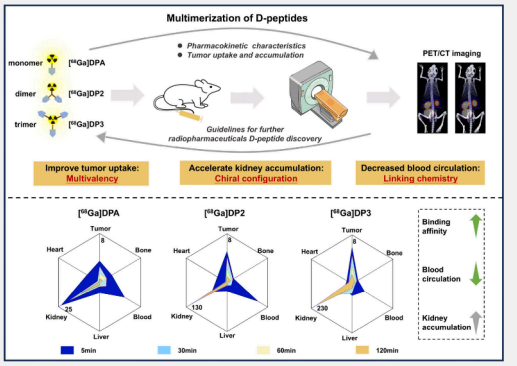


**KEYWORDS:** *D-peptide, PD-L1, pharmacokinetic properties, pharmacodynamic properties, radiopharmaceuticals, PET/CT imaging*

## 1. INTRODUCTION

D-peptides, composed of D-enantiomeric amino acids, are hyper-resistant to proteolytic degradation, leading to enhanced *in vivo* stability and bioavailability.[1] Compared with L-peptides, D-peptides exhibit opposite homochiral configurations at the $\alpha$ carbon adjacent to the carboxyl group,[2,3] resulting in mirror-image structures of their L-counterparts. This unique property allows D-peptides to mimic the binding abilities of L-peptides while remaining unrecognizable to naturally occurring enzymes.[4] As a result, D-peptides are promising candidates as targeting ligands for radiopharmaceuticals, particularly in targeted radionuclide therapy.

The identification of D-peptide ligands for specific proteins can be efficiently achieved using the mirror-image phage display (MIPD) method.[5] In this approach, D-proteins are chemically synthesized and screened against L-peptide ligands. The interactions between L-targets and D-peptides mirror those between D-targets and L-peptides. Consequently, the D-enantiomeric form of an identified L-peptide retains its ability to bind L-targets without compromising binding affinity. Several D-peptide-based radiopharmaceuticals with remarkable *in vivo* performance have been reported to date.[6−8] Notably, our group was the first to track the whole-body *in vivo* behavior of a D-peptide, DPA, which targets the programmed death-1 ligand (PD-L1).[7] This peptide was identified using the MIPD method.[8] Both our finding and human studies by other researchers have demonstrated that DPA is a highly promising ligand for positron emission tomography (PET) imaging of PD-L1 expression levels in patients.

Numerous chemical strategies have been employed to enhance the tumor uptake and accumulation of peptide-based radiopharmaceuticals.[9−14] One widely used approach is multimerization, which increases the binding affinity of radiopharmaceuticals.[15−18] Several multivalent radiopharmaceuticals have demonstrated significant success in clinical trials. For instance, [$^{99m}$Tc]3PRGD2, a single-photon emission computed tomography (SPECT) radiotracer targeting integrins for cancer detection, is currently awaiting regulatory approval. This radiotracer was developed from a divalent RGD peptide.[19] Similarly, radiopharmaceuticals based on fibroblast

**Received:** September 21, 2024
**Revised:** December 9, 2024
**Accepted:** December 31, 2024
**Published:** January 30, 2025

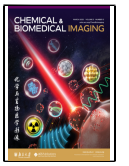

activation protein (FAP) targeting tetramers and prostate specific membrane antigen (PSMA) targeting multimers have shown improved tumor uptake and antitumor efficacy in preclinical studies.[16,20] While multimerization can enhance the pharmacodynamics of radiopharmaceuticals, it can also affect their drug metabolism and pharmacokinetic (DMPK) properties. Previous research has extensively studied the multivalent effects of L-peptide-based radiopharmaceuticals on DMPK. However, the impact of multimerization on the DMPK profiles of D-peptide-based radiopharmaceuticals remains largely unexplored.

Targeted radiopharmaceuticals have achieved significant success in precision medicine.[21−27] These agents can typically be monitored using PET or SPECT scans,[28−34] enabling real-time, dynamic, and noninvasive tracking of their distribution profile. By harnessing PET imaging as a tool, this study aimed to investigate the pharmacokinetic and pharmacodynamic properties of multivalent D-peptide-based radiotracers. Additionally, *ex vivo* biodistribution studies were carried out to validate the imaging results. To explore the multivalent effects, monomeric [$^{68}$Ga]DPA, dimeric [$^{68}$Ga]DP2, and trimeric [$^{68}$Ga]DP3 were synthesized and evaluated in both normal mice and mice bearing PD-L1 overexpressing tumors.[7] Key factors influencing the pharmacodynamics and DMPK of these tracers were analyzed. This study sheds light on the impact of multivalency on the *in vivo* behavior of D-peptides, contributing to the development of D-peptide-based radiotheranostics.

## 2. MATERIALS AND METHODS

### 2.1. Materials

All the chemicals used for synthesis were obtained from J&K Scientific (Beijing, China), Macklin (Shanghai, China), and Titan (Shanghai, China). DPA, DP2, and DP3 peptides were commercially purchased from Shanghai Yaxian Chemical Co., Ltd. Gallium-68 was obtained at Nanjing First Hospital (Nanjing, China) via a $^{68}$Ge/$^{68}$Ga generator (ITM, Munich, Germany). The successful synthesis of the targeting peptides of the radiopharmaceuticals was confirmed by liquid chromatograph mass spectrometer (LC-MS, Waters, Massachusetts, USA). Samples were tested by a radioactive high-performance liquid chromatography (radio-HPLC, Shimadzu, Kyoto, Japan). A 2480 Wizard autogamma counter (PerkinElmer WIZARD2 2480, MA, USA) was used to measure the radioactivity (counts per minute, CPM) for *in vivo* and *in vitro* evaluations.

In this study, we used antibodies including a mouse primary antibody for PD-L1 (Cat no: 66248-1, Proteintech, Rosemont, USA), a rabbit primary antibody for $\beta$-Actin (Cat no: AC038, Abclonal, Wuhan, China), an HRP-labeled anti-mouse secondary antibody (Cat no: AS003, Abclonal, Wuhan, China), an HRP-labeled anti-rabbit secondary antibody (Cat no: AS014, Abclonal, Wuhan, China), and an anti-mouse Alexa Fluor 488 secondary antibody (Cat no: AB150113, Abcam, Cambridge, UK).

### 2.2. Cell Lines and Animals

Mouse melanoma B16F10, human glioblastoma U87MG, and human malignant melanoma A375 cell lines were cultured in a humidified $CO_2$ incubator (37 °C, 5% $CO_2$). The culture medium used was Dulbecco's modified Eagle medium (DMEM, C11995500BT, Thermo Fisher Scientific, Waltham, USA) supplemented with 10% fetal bovine serum (FBS, SE100-011, VISTECH, New South Wales, AUS) and 1% penicillin/streptomycin (SV30010, Cytiva, Uppsala, SE). The cells were passaged when 80−90% confluency was reached.

The animals were humanely cared, and the Animal Ethics Committee of Nanjing Medical University approved all the animal experiments. The mice used in this study were BALB/c-Nude mice unless otherwise indicated. The experiments complied with the guidelines set forth by the Committee for the Care and Use of Laboratory Animals. The mouse models were established according to standard methods. Tumor-bearing mice were injected with $1 \times 10^6$ B16F10 cells/mouse, $3 \times 10^6$ U87MG cells/mouse or $4.4 \times 10^6$ A375 cells/mouse. *In vivo* evaluations were performed on mice with tumor volumes of approximately 100−300 mm$^3$.

### 2.3. Radiolabeling

DPA, DP2, or DP3 peptide (10 $\mu$g) was first dissolved in 0.01 mL of DMSO, and then the peptide solution was placed in 1 mL of 0.25 M sodium acetate. Another 4 mL of 0.05 M hydrochloric acid solution was passed through a $^{68}$Ge/$^{68}$Ga generator to generate a hydrochloric acid solution containing $^{68}$Ga. $^{68}$Ga was mixed with the precursor solution at a ratio of 1:4 and incubated at 100 °C for 10 min. The quality control of the radiotracers was determined via radio-HPLC.

### 2.4. Peptide Stability Assays

*In vitro* stability was assayed by incubating the radiotracers (20 $\mu$Ci/mL) with saline buffer (DPBS, C14190500BT, Thermo Fisher Scientific, Waltham, USA) or mouse serum (ABS937, Absin, Shanghai, China) at 37 °C with agitation for 2 h. After incubation, the samples (20 $\mu$L) were analyzed via radio-HPLC.

For *in vivo* stability analysis, each mouse was injected with a radiotracer (1 mCi/mouse) intravenously. Two hours postinjection (p.i.), urine samples were collected by squeezing; blood samples were collected through the abdominal cavity or orbits. The proteins in the urine and blood samples were precipitated with an equal volume of acetonitrile. After centrifugation (10,000 rpm, 10 min, room temperature (RT)), the supernatant was collected and analyzed via radio-HPLC.

### 2.5. Cellular Uptake and Competitive Binding Experiment

The U87MG cells were plated in 12-well plates and the experiments were conducted until they reached 80% confluency. For the cellular uptake evaluations, [$^{68}$Ga]DPA/[$^{68}$Ga]DP2/[$^{68}$Ga]DP3 (10 $\mu$Ci/mL) was added, and then the cells were maintained at 37 °C for 5, 30, 60, or 120 min. The medium was then removed and the cells were washed with cold PBS three times. Then, 300 $\mu$L NaOH (0.2 M) was used to dissociate the cells, and the cell lysate was collected in a 1.5 mL tube. Autogamma counter was used to measure the radioactivity of the cells.

For the competitive binding assay, unlabeled DPA, DP2, and DP3 were used as competitive inhibitors of [$^{68}$Ga]DPA, [$^{68}$Ga]DP2, and [$^{68}$Ga]DP3, respectively. For the measurement of binding affinity ($K_i$), the radiotracers were co-incubated with different concentrations of their unlabeled precursors for 2 h. The specific uptake of the radiotracer was quantified. Binding affinity was simulated and measured via Prism 8.0.2 software.

### 2.6. Western Blot

B16F10, U87MG, and A375 cells were lysed via radioimmunoprecipitation assay (RIPA, R0010, Solarbio, Beijing, China) buffer, sonicated, and then centrifuged (12000 rpm, 20 min, 4 °C), after which the supernatants were collected. The total protein concentration was measured via a bicinchoninic acid (BCA) Kit (P0012, Beyotime, Shanghai, China). First, electrophoresis was performed via sodium dodecyl sulfate−polyacrylamide gel electrophoresis (SDS−PAGE) at 90 V for 20 min, followed by further electrophoresis for 40 min at 126 V. Then, membrane transfer was performed, and the proteins were transferred to polyvinylidene difluoride (PVDF) membranes for 50 min in an ice bath at 400 mA. After being blocked at RT for 3 h in 5% skim milk, the PVDF membranes were incubated with anti-PD-L1 primary antibody (1:1000, diluted in 5% skim milk) overnight at 4 °C. Then, the secondary antibody (1:5000, diluted in 1% TBST) against the primary antibody was added, and the samples were incubated for 1 h at RT. After the samples were washed three times with 1% Tris-buffered saline with Tween (TBST, T1082, Solarbio, Beijing, China), immunoblotting was performed via a Western blotting detection system after treatment with enhanced chemiluminescence reagent (ECL, E411-04, Nanjing, China).


https://doi.org/10.1021/cbmi.4c00071
Chem. Biomed. Imaging 2025, 3, 180−190

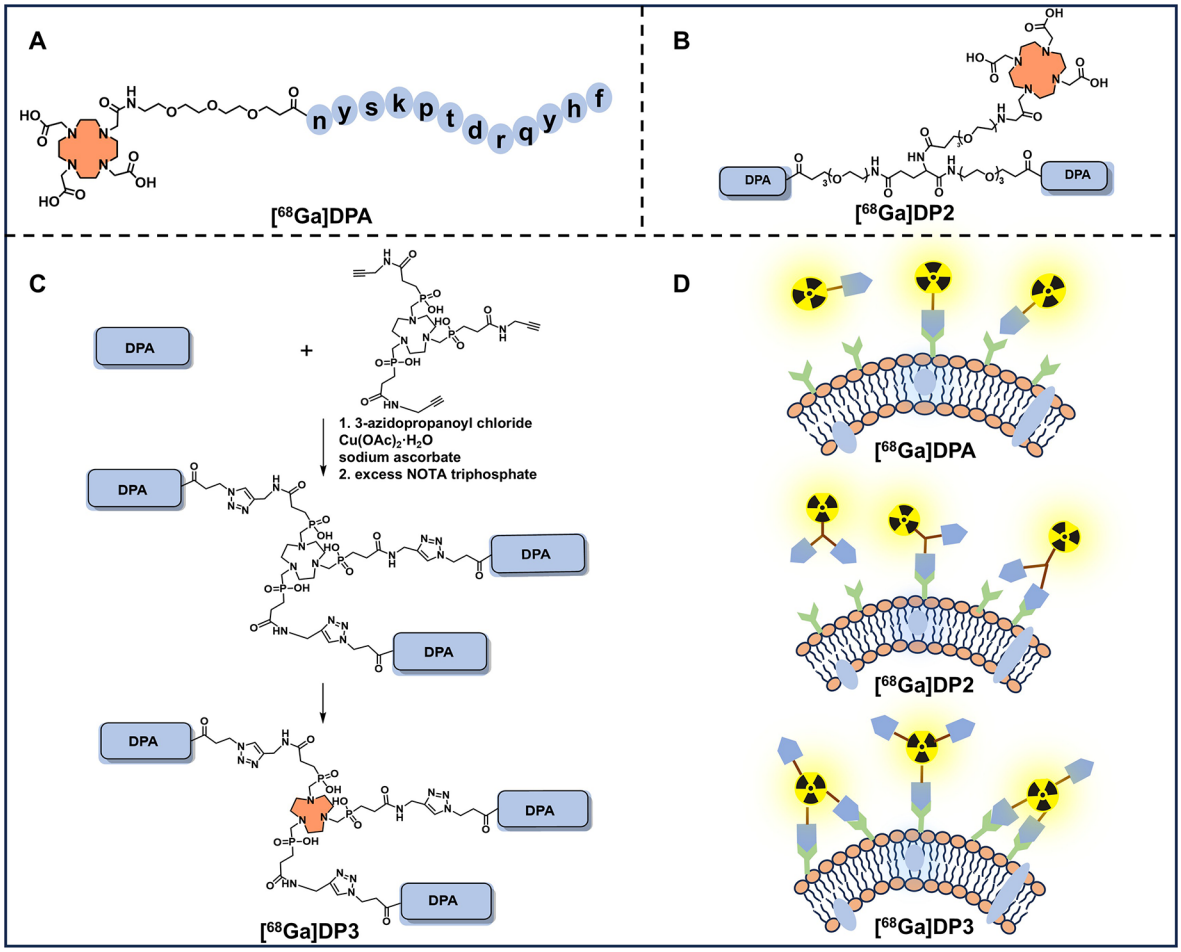


**Figure 1.** Schematic diagram of the chemical structures and binding patterns of [$^{68}$Ga]DPA, [$^{68}$Ga]DP2, and [$^{68}$Ga]DP3. (A) Schematic structure of the monomer [$^{68}$Ga]DPA. The peptide is connected to a DOTA through a $PEG_3$ linker. (B) Schematic structure of dimeric [$^{68}$Ga]DP2. (C) Synthetic flowchart of trimeric [$^{68}$Ga]DP3. The orange part is the site for $^{68}$Ga chelation. (D) Proposed binding patterns of monomeric [$^{68}$Ga]DPA, dimeric [$^{68}$Ga]DP2, and trimeric [$^{68}$Ga]DP3 to PD-L1 on the tumor cell surface. Higher valency is expected to have greater binding ability.

### 2.7. Flow Cytometry Analysis of PD-L1 Expression

The cells (B16F10, U87MG, and A375) were dissociated and collected into two 1.5 mL EP tubes, one tube for the negative control and another for PD-L1 expression measurement. The cells were fixed with 1% paraformaldehyde (PFA, BL539A, Biosharp, Anhui, China) at RT for 15 min, and then permeated with 0.2% Tween-20 (R0010, Solarbio, Beijing, China). An anti-mouse antibody against PD-L1(1:500, diluted in 3% BSA) was added, and the mixture was incubated for 1 h at 4 °C, followed by washing three times with DPBS. The samples were subsequently washed three times with 3% bovine serum albumin V (BSA-V, A8020, Solarbio, Beijing, China). The anti-mouse Alexa Fluor 488 secondary antibody (1:2000, diluted in 3% BSA) was add, and the mixture was incubated for 30 min at 4 °C. Analysis was performed via Attune NxT Acoustic Focusing Cytometer (Thermo Fisher Scientific, Waltham, USA). The results were analyzed via FlowJo 10.8.1 software.

### 2.8. Small Animal PET/CT Study in Normal Mice

Small animal PET/CT imaging was performed via Inveon Micro-PET/CT (Siemens Medical Solutions, Knoxville, Munich, Germany). Each mouse (n = 3) was injected with 100 $\mu$Ci of [$^{68}$Ga]DPA, [$^{68}$Ga]DP2, or [$^{68}$Ga]DP3 intravenously. Dynamic PET/CT imaging was performed in normal mice, which started immediately after the injection and lasted for 60 min. The results were analyzed for 0−5 min, 6−15 min, 16−30 min, 31−45 min, and 46−60 min. The radioactivity was decay-corrected to the injection time and presented as a percentage of the total injection dose per gram (%ID/g).

### 2.9. Small Animal PET/CT Study in Tumor-Bearing Mice

Three kinds of tumor-bearing mice (B16F10, U87MG, and A375) were injected with 100 $\mu$Ci/mouse (n = 3) via the tail vein, and a series of PET/CT scans was performed at 30, 60, 120, and 240 min p.i. for the B16F10 tumor-bearing mice; and at 30, 60, and 120 min for the U87MG tumor-bearing mice; and at 30 and 60 min for the A375 tumor-bearing mice. For blocking experiments, PD-L1 was blocked with BMS-1 (500 $\mu$g/mL; 100 $\mu$L; p.i.), and [$^{68}$Ga]DPA, [$^{68}$Ga]DP2 or [$^{68}$Ga]DP3 was injected 5 min later. The decay-corrected %ID/g of tumors and each organ was then calculated.

### 2.10. *Ex Vivo* Biodistribution

The radiotracers [$^{68}$Ga]DPA, [$^{68}$Ga]DP2, or [$^{68}$Ga]DP3 were injected intravenously into normal mice and U87MG tumor-bearing mice (50 $\mu$Ci/mouse, n = 3). Three mice were sacrificed at 5, 30, 60, and 120 min p.i. after being treated with isoflurane. The tumors, blood, and major organs were dissected, wet weighed, and applied to the autogamma counter to measure the radioactivity of the organs. The decay-corrected %ID/g of each organ was then calculated.

### 2.11. Statistical Analysis

Each data point represents the mean ± SD of at least three independent experiments ($n \geq 3$) with normally distributed characteristics. Statistical data were analyzed using GraphPad Prism 8.0.2, based on student $t$ test. Data were considered statistically significant at $p$ values <0.05.



https://doi.org/10.1021/cbmi.4c00071
Chem. Biomed. Imaging 2025, 3, 180−190

## 3. RESULTS AND DISCUSSION

### 3.1. Synthesis and *In Vitro* Evaluation of [$^{68}$Ga]PDA, [$^{68}$Ga]DP2, and [$^{68}$Ga]DP3

The dimeric peptide DP2 and the trimeric peptide DP3 were designed based on our previously reported PD-L1-targeted D-peptide, DPA (Figure 1A–C).[7] The sequence of the DPA peptide is nyskptdrqyhf, conjugated with the chelator DOTA. DPA was linked to DOTA via a miniPEG$_3$ chain and a glutamate residue to form the dimeric peptide DP2 (Figure 1A,B, Figure S1). DP3, on the other hand, was linked via click chemistry using the TRAP chelator (Figure 1C, Figure S2).[18,35] The molecular weights of DPA, DP2, and DP3 were 2143.3, 4216.6, and 5648.8, respectively, as determined by LC–MS (Figures S3 and S4, Table S1). These three D-peptide precursors were labeled with $^{68}$Ga, producing [$^{68}$Ga]-DPA, [$^{68}$Ga]DP2, and [$^{68}$Ga]DP3, which achieved radiochemical yields (RCYs) greater than 98% (Table 1, and Figure S5–S7).

**Table 1. Radiochemical Yields and Chelators of the Radiotracers**[a]

| Radiotracer | [$^{68}$Ga]DPA | [$^{68}$Ga]DP2 | [$^{68}$Ga]DP3 |
|---|---|---|---|
| radiochemical yield (RCY) | 98% | 98% | 98% |
| chelator | DOTA | DOTA | TRAP |

[a]The radiochemical yields of the radiotracers used in this study were greater than 98%. The chelators used for labeling these radiotracers are listed in the table. The radiochemical yields were determined by radio-HPLC. The chromatographic column used was a YMC-Triat-C18 column (4.6 mm inner diameter, 150 mm length, 5 $\mu$m particle size). The solvent gradient was as follows: solvent A, aqueous solution with 0.1% trifluoroacetic acid (TFA); solvent B, acetonitrile with 0.1% TFA. The data were acquired over 15 min, with acetonitrile concentration increasing from 20% to 90%, and the flow rate was set to 1 mL/min.

The main purpose of the multimerization strategy is to enhance the binding capacity to target proteins (Figure 1D). To evaluate this, the binding affinities of [$^{68}$Ga]DPA, [$^{68}$Ga]DP2, and [$^{68}$Ga]DP3 to PD-L1 on U87MG tumor cells were assessed. A time-dependent uptake of the three radiotracers was observed (Figure 2A). Additionally, a competitive binding assay was performed, with different concentrations of a precursor used to block PD-L1 (Figure 2B). The inhibition constants ($K_i$) for [$^{68}$Ga]DPA, [$^{68}$Ga]DP2, and [$^{68}$Ga]DP3 were 115.9 nM, 110.5 nM, and 93.66 nM, respectively. These results suggest that the cell uptake of the multivalent radiotracers, [$^{68}$Ga]DP2 and [$^{68}$Ga]DP3, was greater than that of [$^{68}$Ga]DPA.

### 3.2. PET/CT Evaluation of Tumor Uptake in Different Tumor-Bearing Mice

PET/CT scans of [$^{68}$Ga]DPA, [$^{68}$Ga]DP2, and [$^{68}$Ga]DP3 were performed in three tumor-bearing mouse models: U87MG, B16F10, and A375. Western blotting and flow cytometry confirmed PD-L1 expression in these three cell lines (Figure 2C–E), with the highest expression detected in B16F10 cells. PET/CT imaging showed significant radiotracer uptake in all three PD-L1-expressing tumor models within 60 min p.i. (Figure 3A). Quantitative PET/CT imaging data revealed that tumor uptake of [$^{68}$Ga]DP3 was greater than that of [$^{68}$Ga]DPA and [$^{68}$Ga]DP2 in all three tumor models at each time point (Figure 3B).

Notably, the uptake profiles differed across the three tumor-bearing mouse strains. Tumor uptake of both [$^{68}$Ga]DP2 and [$^{68}$Ga]DP3 was increased in the B16F10 tumor allografts, with [$^{68}$Ga]DP3 showing the highest uptake, consistent with *in vitro* results. However, although uptake of [$^{68}$Ga]DP3 improved in U87MG xenograft, no significant difference was observed between [$^{68}$Ga]DPA and [$^{68}$Ga]DP2. Additionally, increased tumor uptake of [$^{68}$Ga]DP2 was observed only at 60 min p.i. in A375 xenografts (Figure 3B).

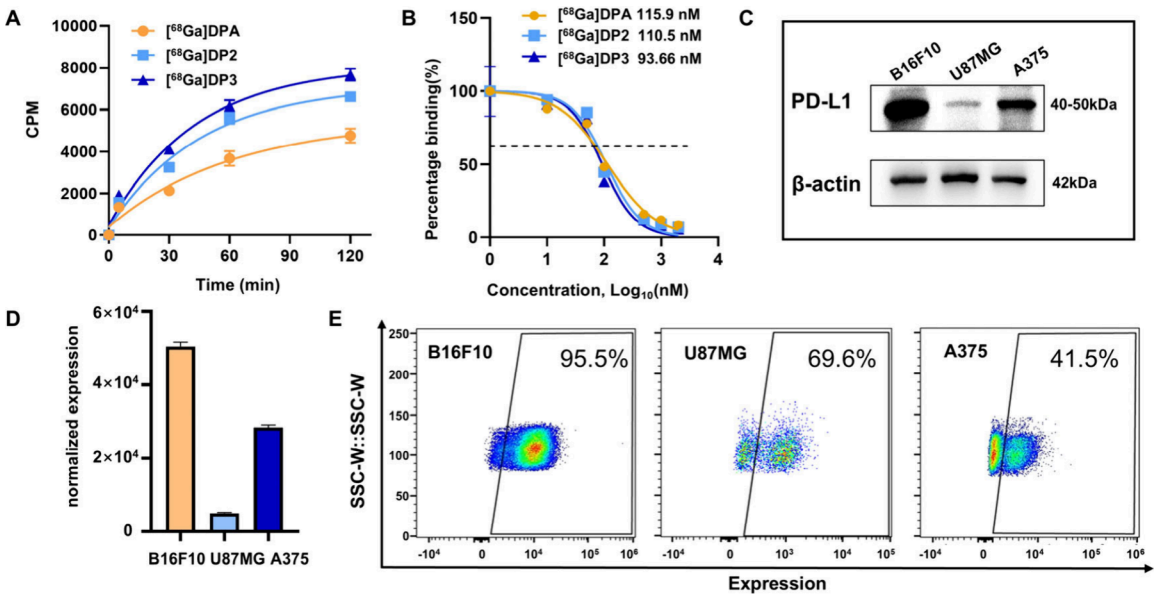


**Figure 2.** Expression of PD-L1 and *in vitro* assessment of [$^{68}$Ga]DPA, [$^{68}$Ga]DP2, and [$^{68}$Ga]DP3. (A) The uptake of [$^{68}$Ga]DPA, [$^{68}$Ga]DP2, and [$^{68}$Ga]DP3 in the U87MG cell line showed a time-dependent pattern. (B) Competitive binding of [$^{68}$Ga]DPA, [$^{68}$Ga]DP2, and [$^{68}$Ga]DP3 was evaluated in the U87MG cell line. (C, D) PD-L1 expression was verified by Western blot (C) and quantification (D) in three cell lines, with the highest expression detected in the B16F10 cells. (E) PD-L1 expression was also analyzed by flow cytometry in the U87MG, B16F10, and A375 cell lines, showing the highest expression in the B16F10 cells. The data are presented as means ± SD; $n$ = 3.


https://doi.org/10.1021/cbmi.4c00071
Chem. Biomed. Imaging 2025, 3, 180–190

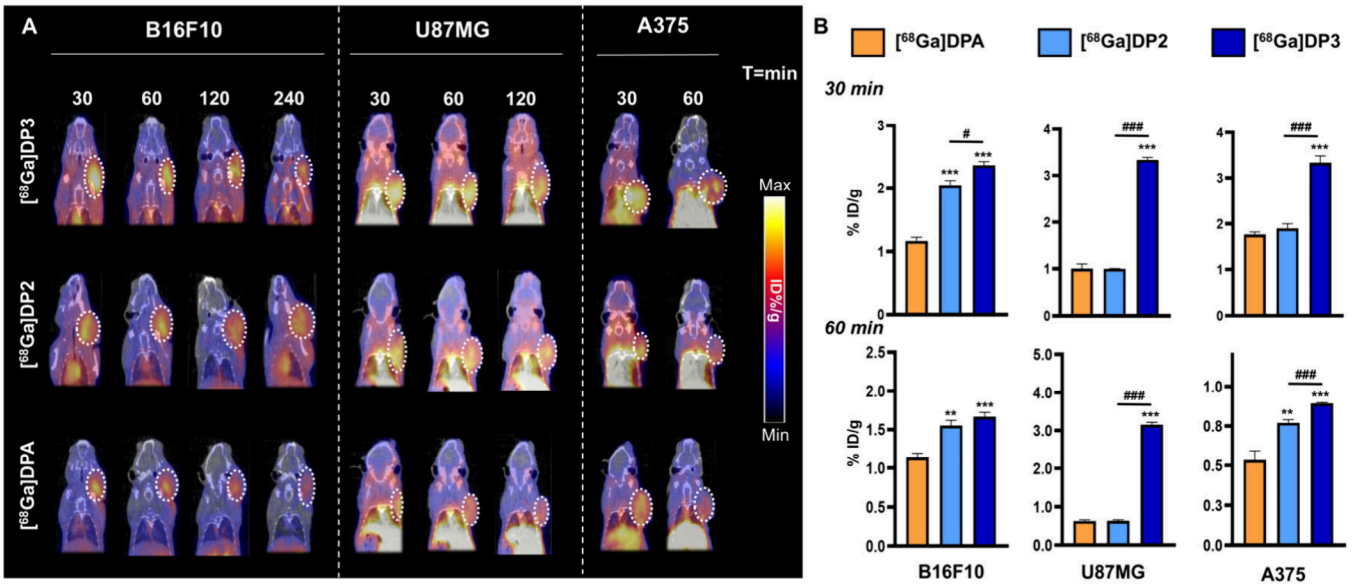


**Figure 3.** PET/CT imaging of [$^{68}$Ga]DPA, [$^{68}$Ga]DP2, and [$^{68}$Ga]DP3 in tumor-bearing mice. (A) PET/CT images of [$^{68}$Ga]DPA, [$^{68}$Ga]DP2, and [$^{68}$Ga]DP3 in B16F10, U87MG, and A375 tumor-bearing mice. Mice were injected with 100 $\mu$Ci/mouse via the tail vein. B16F10 tumor-bearing mice were imaged at 30, 60, 120, and 240 min p.i.; U87MG tumor-bearing mice were imaged at 30, 60, and 120 min p.i.; and A375 tumor-bearing mice were imaged at 30 and 60 min p.i. The dashed circles indicate the tumors. (B) Tumor uptake in the B16F10, U87MG, and A375 tumor-bearing mice were quantified based on PET/CT imaging of [$^{68}$Ga]DPA, [$^{68}$Ga]DP2, and [$^{68}$Ga]DP3 at 30 and 60 min p.i.. #$p$ < 0.05, **/##$p$ < 0.01, ***/###$p$ < 0.001. * indicates comparison with [$^{68}$Ga]DPA. # indicates a comparison between [$^{68}$Ga]DP2 and [$^{68}$Ga]DP3. The data are presented as means ± SD; $n$ = 3.

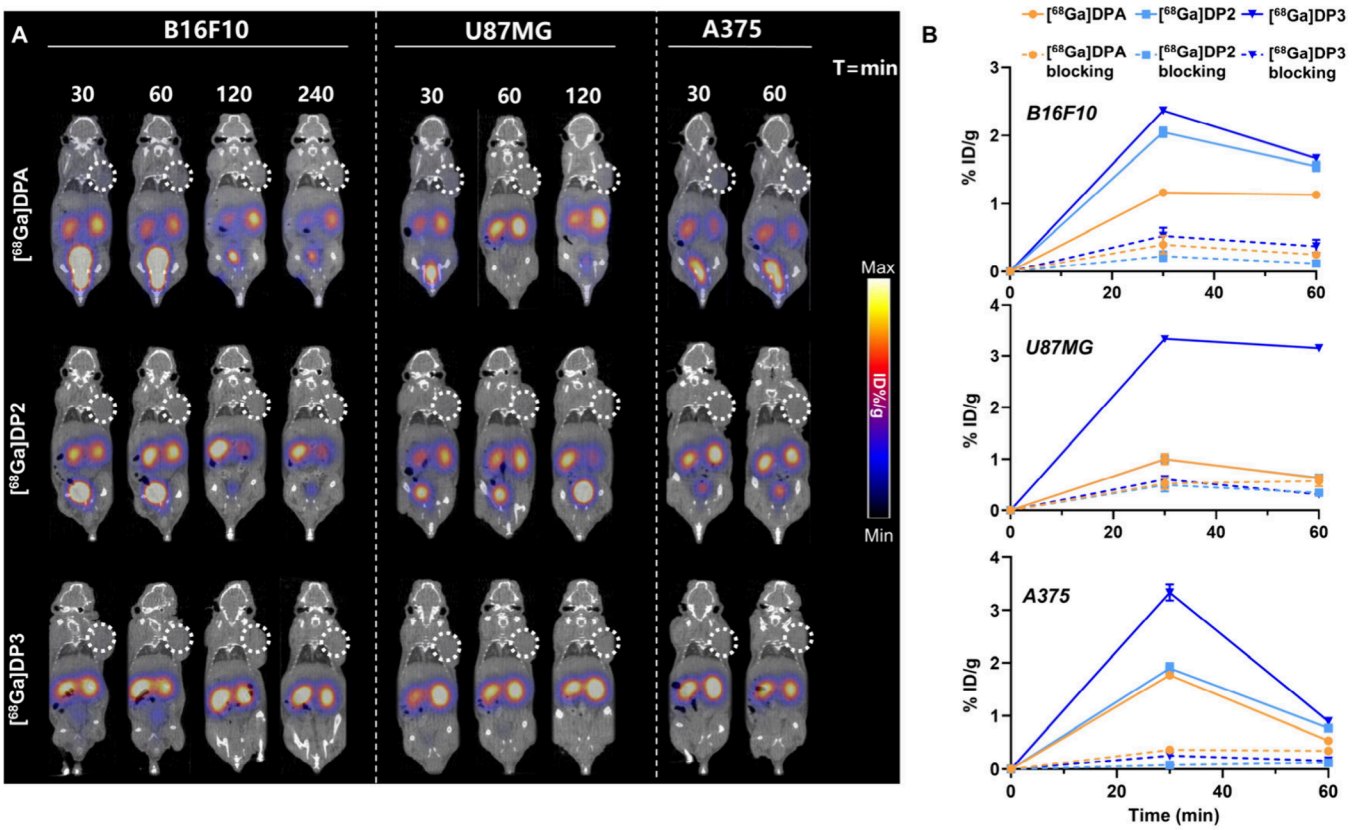


**Figure 4.** Blocking studies of [$^{68}$Ga]DPA, [$^{68}$Ga]DP2, and [$^{68}$Ga]DP3 in tumor-bearing mice. (A) B16F10, U87MG, and A375 tumor-bearing mice were first injected with the PD-L1 inhibitor BMS-1, followed by injection of [$^{68}$Ga]DPA, [$^{68}$Ga]DP2, or [$^{68}$Ga]DP3 for PET/CT imaging. The data acquisition times were the same as those used for PET/CT imaging of tumor-bearing mice in Figure 3A. (B) Quantitative results at 30 and 60 min, based on both standard and blocking PET/CT imaging in B16F10, U87MG and A375 tumors. The solid line represents tumor uptake in nonblocked mice, while the dotted line represents the blocking results. Data are presented as means ± SD, $n$ = 3.



https://doi.org/10.1021/cbmi.4c00071
Chem. Biomed. Imaging 2025, 3, 180−190

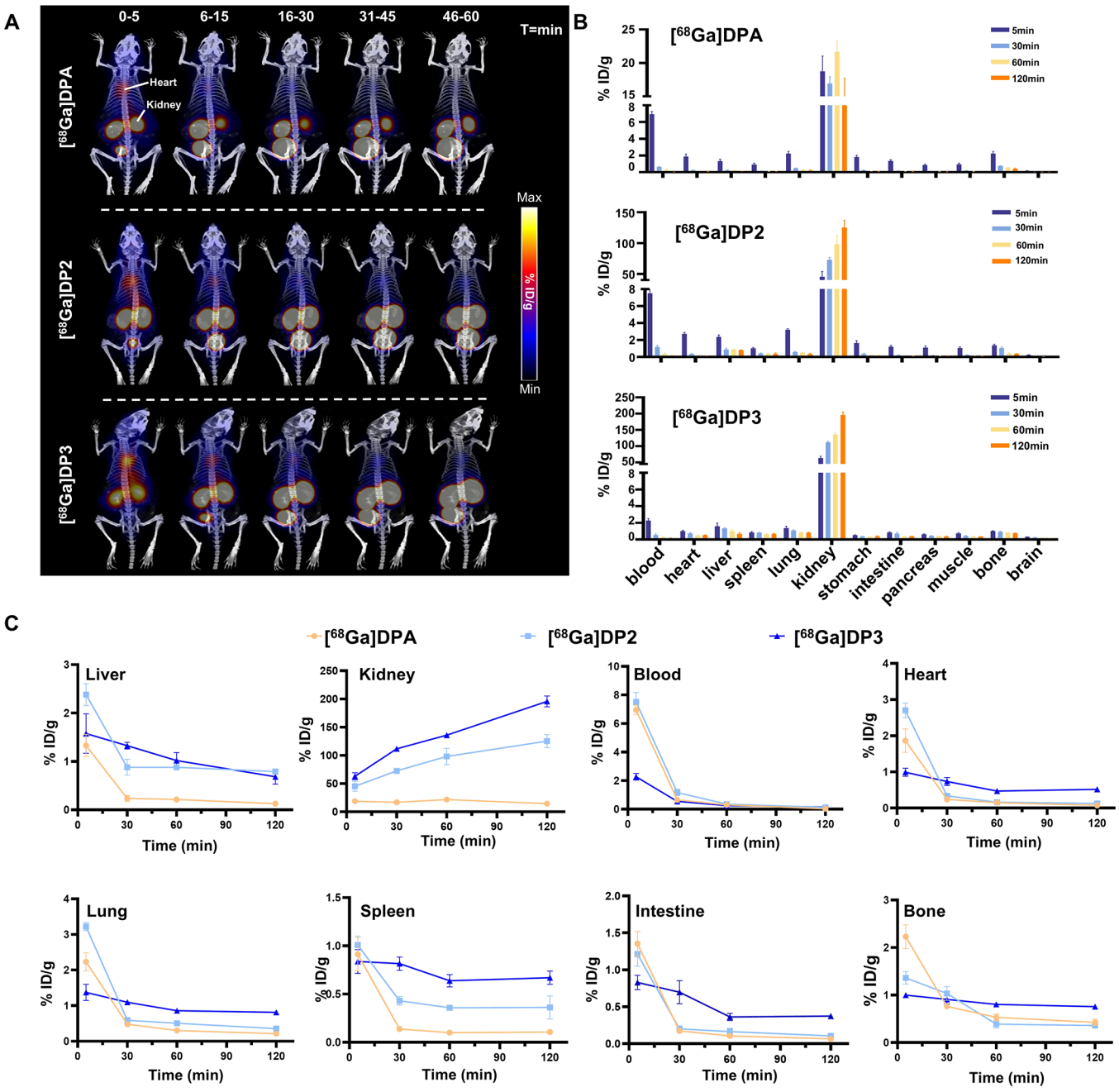


**Figure 5.** Dynamic PET/CT imaging and *ex vivo* biodistribution analysis of [$^{68}$Ga]DPA, [$^{68}$Ga]DP2, and [$^{68}$Ga]DP3 in normal mice. (A) Dynamic PET/CT imaging of the three radiotracers in normal mice. Mice were injected with 100 $\mu$Ci/mouse of [$^{68}$Ga]DPA, [$^{68}$Ga]DP2, or [$^{68}$Ga]DP3 via the tail vein, then immediately subjected to a 60-min dynamic PET/CT scan. (B) *Ex vivo* biodistribution studies of radiotracers in normal mice. Mice were intravenously injected with 50 $\mu$Ci/mouse of each radiotracer. Blood, heart, liver, spleen, lung, kidney, stomach, intestine, pancreas, muscle, bone, and brain samples were collected at 5, 30, 60, and 120 min p.i. and analyzed with an autogamma counter to measure radioactivity. (C) Analysis of changes in uptake over time in eight major organs. Liver uptake was low overall, while kidney uptake showed a significant increase. The data are presented as means ± SD; $n$ = 3.

The differences in tumor uptake may be attributed to varying levels of PD-L1 expression and different across the three cell lines. B16F10 cells exhibited the highest PD-L1 expression, A375 cells showed moderate expression, and U87MG cells had low expression. Additionally, since DPA was developed using human PD-L1 for screening, the species difference between B16F10 (a mouse cell line) and human PD-L1 may reduce DPA' s ability to recognize mouse PD-L1. Previous studies have reported that DPA has good affinity and specificity for human PD-L1, and that multimerization may not alter these properties.[6−8] Nonetheless, the tumor uptake of [$^{68}$Ga]DP3 was consistently higher in all three tumor models, indicating that the trimerized D-peptide had an enhanced binding affinity for PD-L1.

To further confirm the specific binding of the radiotracers, [$^{68}$Ga]DPA, [$^{68}$Ga]DP2, and [$^{68}$Ga]DP3 were co-injected with excess of BMS-1, a PD-L1 inhibitor, for blocking PET-CT imaging study (Figure 4A). Quantitative data for tumor uptake of the three radiotracers at 30 and 60 min p.i. were collected (Figure 4B). Tumor uptake of all three radiotracers was


https://doi.org/10.1021/cbmi.4c00071
Chem. Biomed. Imaging 2025, 3, 180−190

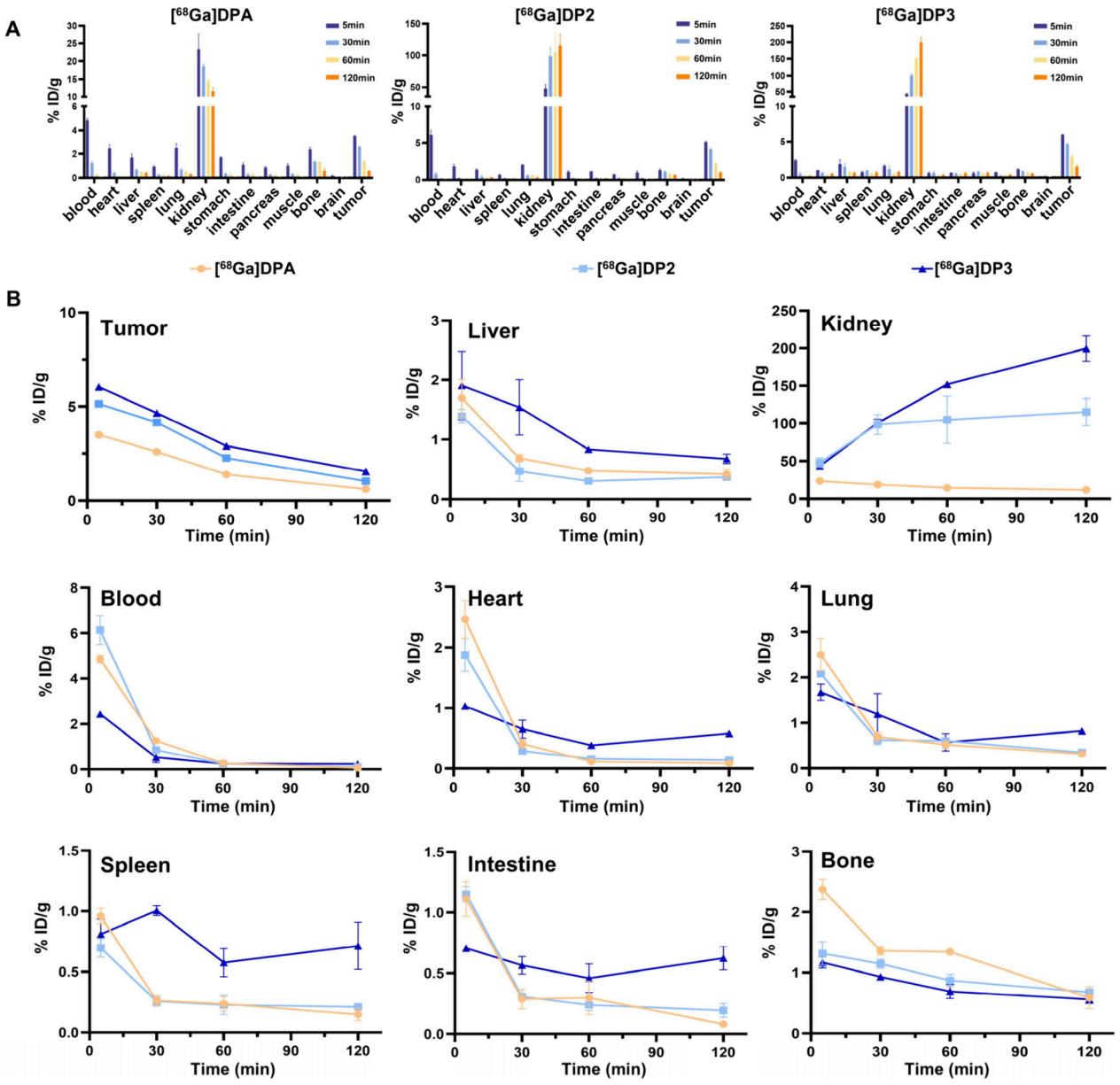


**Figure 6.** *Ex vivo* biodistribution analysis of [$^{68}$Ga]DPA, [$^{68}$Ga]DP2, and [$^{68}$Ga]DP3 in tumor-bearing mice. (A) *Ex vivo* biodistribution studies of radiotracers in tumor-bearing mice. U87MG tumor model mice were injected with 50 $\mu$Ci/mouse via the tail vein; At 5, 30, 60, and 120 min p.i., blood, heart, liver, spleen, lung, kidneys, stomach, intestines, pancreas, muscle, bone, brain, and tumors were harvested and analyzed for radioactivity distribution with a autogamma counter. (B) Tumor and major organ uptake over time. Tumor uptake was enhanced with multimerization. Uptake in the other organs showed slightly difference compared to normal mice. The data are presented as means ± SD; $n$ = 3.

significantly reduced after PD-L1 blockade, further demonstrating the specificity of their binding to PD-L1 (Figure 4A,B).

### 3.3. Analysis of [$^{68}$Ga]DPA, [$^{68}$Ga]DP2, and [$^{68}$Ga]DP3 in Normal Mice and Tumor Bearing Mice

To investigate the effects of multimerization on pharmacokinetic characteristics, we first performed dynamic PET/CT scans of the three radiotracers in normal mice within 60 min p.i. PET/CT imaging showed that [$^{68}$Ga]DPA, [$^{68}$Ga]DP2, and [$^{68}$Ga]DP3 were primarily excreted via renal metabolism, with minimal accumulation in the liver (Figure 5A). This finding was consistent with the *ex vivo* biodistribution analysis in normal mice (Figure 5B). The data were analyzed for uptake in eight major organs: liver, kidney, blood, heart, lung, spleen, intestine, and bone (Figure 5C). Compared to the monomer [$^{68}$Ga]DPA, both the dimer [$^{68}$Ga]DP2 and the trimer [$^{68}$Ga]DP3 showed a significant increase in kidney uptake. However, in the blood, [$^{68}$Ga]DP2 and [$^{68}$Ga]DP3 exhibited different patterns, with [$^{68}$Ga]DP2 showing slight increased uptake, while [$^{68}$Ga]DP3 showed decreased uptake. Uptake tendency in the heart, lung, spleen, intestine, and bone was similar for all three radiotracers, with slight increases observed for [$^{68}$Ga]DP2 and [$^{68}$Ga]DP3, but lower uptake at 5 min p.i.

*Ex vivo* biodistribution studies of [$^{68}$Ga]DPA, [$^{68}$Ga]DP2, and [$^{68}$Ga]DP3 were also performed in U87MG tumor-bearing mice (Figure 6A). The organ uptake in tumor-bearing mice was generally similar to that observed in normal mice (Figures 5C, 6B). The highest tumor uptake was observed with [$^{68}$Ga]DP3, which decreased over time, consistent with PET/CT imaging findings. The low liver uptake of all three radiotracers suggests that multimerization did not significantly


https://doi.org/10.1021/cbmi.4c00071
Chem. Biomed. Imaging 2025, 3, 180−190

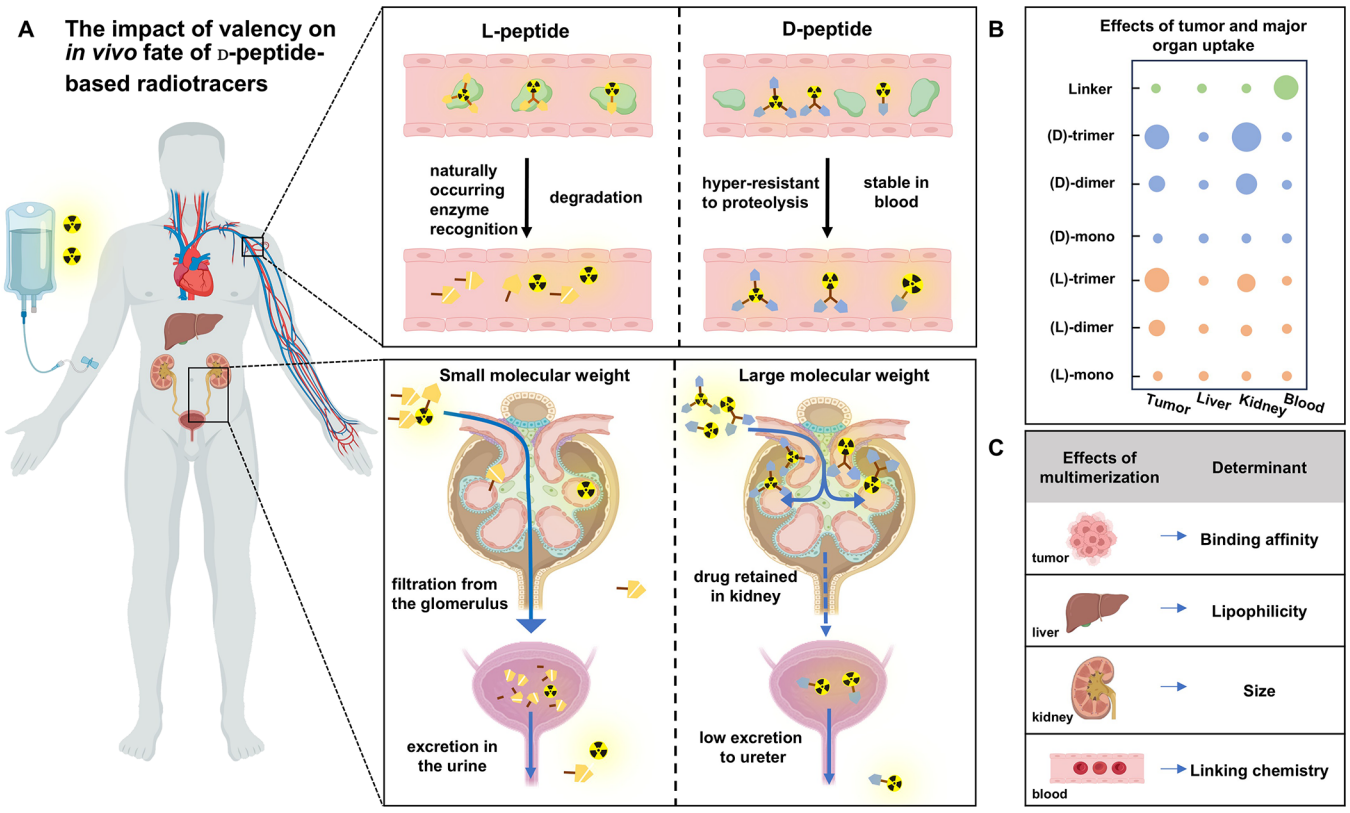


**Figure 7.** Effect of valency on the *in vivo* fate of D-peptide and L-peptide radiotracers. (A) Schematic illustration of the degradation and excretion of L-peptide and D-peptide in the blood and kidneys. L-Peptides are prone to degradation in the blood and are rapidly eliminated by the kidneys. In contrast, D-peptide cannot be recognized or degraded by proteases, giving them enhanced *in vivo* stability. Due to their large size, D-peptides are slowly eliminated by the kidneys. (B) Effect of uptake in tumors and major organs. Tumor uptake is primarily increased through multimerization. Liver uptake is unaffected by the linkers, chirality, or multimerization. D-Peptide-based radiotracers show a greater impact on kidney uptake compared to their L-peptide counterparts. Blood toxicity is strongly influenced by linking chemistry. (C) Effects of multimerization on tumors and major organs, along with their corresponding determinants. Tumor uptake is influenced by binding affinity, liver uptake is influenced by lipophilicity, kidney excretion is related to peptide size, and blood toxicity is influenced by linking chemistry. Part of the images were created using Biorender.

affect the lipophilicity of D-peptides, which is a key factor in determing the liver retention. In the kidneys, both normal and tumor-bearing mice showed significantly increased uptake of [$^{68}$Ga]DP2 and [$^{68}$Ga]DP3. The uptake of [$^{68}$Ga]DP2 increased rapidly at 30 min p.i., followed by a slower rise (Figure 6B). Uptake in the blood and heart was similar to that observed in normal mice. The intestinal uptake of [$^{68}$Ga]DP3 was higher than that of [$^{68}$Ga]DP2 and [$^{68}$Ga]DPA at 30 min p.i., but not at 5 min p.i. (Figure 6B), consistent with findings in normal mice. Increased uptake of [$^{68}$Ga]DP3 was observed in the lungs at 120 min p.i., which was different from the pattern in normal mice. Notable differences in biodistribution were observed between tumor-bearing mice and normal mice, suggesting that cancer may influence the physiological characteristics and functions of major organs (Figure 5A,B).

Multimerized D-peptide-based radiotracers, particularly the trimerized [$^{68}$Ga]DP3, primarily accumulated in tumors, indicating that multimerization enhances binding affinity, similar to the effects observed with L-peptides (Figure 7). No significant increase in blood accumulation was observed for either [$^{68}$Ga]DP2 or [$^{68}$Ga]DP3, which contradicts the conventional theory that multimerization leads to prolonged blood circulation and long-acting effects. A slight increase in blood accumulation was noted for [$^{68}$Ga]DP2, likely due to the PEG chain-based linker, which can bind to albumin, slowing its clearance from the bloodstream.[36] In contrast, the blood uptake of [$^{68}$Ga]DP3, which used a click chemistry-based linker (TRAP) without PEG chains, was significantly lower than those of [$^{68}$Ga]DPA and [$^{68}$Ga]DP2. These results underscore the importance of linker chemistry in modulating the *in vivo* pharmacokinetic of multimerized peptides (Figure 7B,C).

Furthermore, the residence of radiotracers in the blood can also be influenced by changes in their original lipophilicity. Covalent radiotracers can bind to blood proteins, which may increase their retention in the bloodstream. This study suggests that linkers based on click chemistry and PEG-free designs may be more advantageous in terms of biosafety. The appropriate choice of linker chemistry for developing multivalent peptide-based radiopharmaceuticals could increase tumor accumulation while minimizing blood toxicity, a key concern in clinical radiopharmaceuticals.

The overall effect of multimerization on liver uptake and other major organs was not significant, indicating that multivalency does not substantially alter the physicochemical properties of D-peptides, particularly their lipophilicity. However, multivalency significantly increased kidney uptake, with a greater effect than observed for multivalent L-peptide.[37−43] This is likely due to the larger molecular size of the dimer and trimer radiotracers, which affects their


https://doi.org/10.1021/cbmi.4c00071
Chem. Biomed. Imaging 2025, 3, 180−190

glomerular filtration rate. Peptides or proteins larger than 35 Å are less efficiently filtered from the glomerulus into the ureter. Multimerized D-peptides, which are more resistant to proteases degradation, have a larger hydrodynamic size, leading to increased retention in the kidneys but less clearance into the bladder (Figure 7A).

Increased kidney accumulation may raise concerns about nephrotoxicity, suggesting that strategies aimed at enhancing kidney excretion and providing kidney protection should be considered in the further development of D-peptide-based radiopharmaceuticals.[44,45] For example, peptide sequence modification/insertion (e.g., inserting MVK tripeptide to the N-terminal of peptides) during radiopharmaceutical development can be considered for facilitating renal excretion.[44] Moreover, coadministration of kidney-protective agents, such as succinylated gelatin, could help improve renal metabolism and reduce toxicity.[45]

## 4. CONCLUSIONS

This study provides valuable insights into how the multimerization of D-peptide-based radiopharmaceuticals influences their *in vivo* pharmacokinetic and pharmacodynamic properties. While multivalency significantly increased tumor uptake, its primary impact was observed in kidney accumulation, which depends on the chiral configuration of amino acids. Changes in blood uptake further emphasized the critical role of linking chemistry in shaping the *in vivo* performance of these radiopharmaceuticals. Notably, multivalency had minimal effects on other major organs, underscoring the biosafety of multimerized D-peptides. The findings presented in this study offer crucial guidance for developing multimerized D-peptide radiopharmaceuticals and represent an important step toward the discovery of effective radiotheranostics.

## ■ ASSOCIATED CONTENT

### Supporting Information

The Supporting Information is available free of charge at https://pubs.acs.org/doi/10.1021/cbmi.4c00071.

Chemical structures of DP2 and DP3; confirmation of the synthesis results based on LC-MS and HPLC analysis; and quality control data of [$^{68}$Ga]DPA, [$^{68}$Ga]DP2, and [$^{68}$Ga]DP3 (PDF)

## ■ AUTHOR INFORMATION


### Corresponding Authors

**Rui Wang** − *State Key Laboratory of Bioactive Substance and Function of Natural Medicines, Institute of Materia Medica, Chinese Academy of Medical Sciences and Peking Union Medical College, Beijing 100050, China; Key Laboratory of Preclinical Study for New Drugs of Gansu Province, School of Basic Medical Sciences & Research Unit of Peptide Science, Chinese Academy of Medical Sciences, Lanzhou University, Lanzhou 730000, China;* orcid.org/0000-0002-4719-9921; Email: wangrui@lzu.edu.cn

**Kuan Hu** − *State Key Laboratory of Bioactive Substance and Function of Natural Medicines, Institute of Materia Medica, Chinese Academy of Medical Sciences and Peking Union Medical College, Beijing 100050, China;* orcid.org/0000-0003-2448-2254; Email: hukuan@imm.ac.cn

### Authors

**Siqi Zhang** − *State Key Laboratory of Bioactive Substance and Function of Natural Medicines, Institute of Materia Medica, Chinese Academy of Medical Sciences and Peking Union Medical College, Beijing 100050, China*

**Xiaona Sun** − *State Key Laboratory of Bioactive Substance and Function of Natural Medicines, Institute of Materia Medica, Chinese Academy of Medical Sciences and Peking Union Medical College, Beijing 100050, China*

**Wenhao Liu** − *State Key Laboratory of Bioactive Substance and Function of Natural Medicines, Institute of Materia Medica, Chinese Academy of Medical Sciences and Peking Union Medical College, Beijing 100050, China*

**Jiang Wu** − *Department of Nuclear Medicine, Nanjing First Hospital, Nanjing Medical University, Nanjing 210008, China*

**Yuxuan Wu** − *State Key Laboratory of Bioactive Substance and Function of Natural Medicines, Institute of Materia Medica, Chinese Academy of Medical Sciences and Peking Union Medical College, Beijing 100050, China*

**Shuo Jiang** − *State Key Laboratory of Bioactive Substance and Function of Natural Medicines, Institute of Materia Medica, Chinese Academy of Medical Sciences and Peking Union Medical College, Beijing 100050, China*

**Xingkai Wang** − *State Key Laboratory of Bioactive Substance and Function of Natural Medicines, Institute of Materia Medica, Chinese Academy of Medical Sciences and Peking Union Medical College, Beijing 100050, China*

**Xin Gao** − *State Key Laboratory of Bioactive Substance and Function of Natural Medicines, Institute of Materia Medica, Chinese Academy of Medical Sciences and Peking Union Medical College, Beijing 100050, China*

**Quan Zuo** − *State Key Laboratory of Bioactive Substance and Function of Natural Medicines, Institute of Materia Medica, Chinese Academy of Medical Sciences and Peking Union Medical College, Beijing 100050, China;* orcid.org/0000-0002-4451-3380

**Hailong Zhang** − *Key Laboratory of Preclinical Study for New Drugs of Gansu Province, School of Basic Medical Sciences & Research Unit of Peptide Science, Chinese Academy of Medical Sciences, Lanzhou University, Lanzhou 730000, China*

**Yingzi Zhang** − *Department of Orthopaedics, the Second Affiliated Hospital of Soochow University, Suzhou 215004 Jiangsu, China*

**Feng Wang** − *Department of Nuclear Medicine, Nanjing First Hospital, Nanjing Medical University, Nanjing 210008, China*

Complete contact information is available at: https://pubs.acs.org/10.1021/cbmi.4c00071

### Author Contributions

▽Z.S., S.X., and L.W. contributed equally to this work.


### Notes

The authors declare no competing financial interest.

## ■ ACKNOWLEDGMENTS

This study was supported by the National Natural Science Foundation of China (No. 82372002), the Nonprofit Central Research Institute Fund of the Chinese Academy of Medical Sciences (No. 2022-RC350-04), the CAMS Innovation Fund

for Medical Sciences (Nos. 2021-I2M-1-026, 2022-I2M-2-002-2, 2021-I2M-3-001, 2023-12M-2-006, and 2023-12M-QJ-010), and the Beijing Nova Program and Beijing Nova Programme Interdisciplinary Cooperation Project to K.H. This work was also supported by the Beijing Natural Science Foundation (Nos. L246051, L234044 and L248087), the Fundamental Research Funds for the Central Universities (Nos. 3332023044 and 3332023151), the CIRP Open Fund of Radiation Protection Laboratories (No. ZHYLYB2021005), and the China National Nuclear Corporation Young Talent Program.

## REFERENCES

(1) Pasteur, L. Recherches sur la dissymétrie moléculaire des produits organiques naturels. *Lecons Professees a la Societe Chimique de Paris*; 1861.
(2) Prelog, V. Chirality in chemistry. *Science* **1976**, *193* (4247), 17−24.
(3) Hu, K.; Jiang, Y.; Xiong, W.; Li, H.; Zhang, P.-Y.; Yin, F.; Zhang, Q.; Geng, H.; Jiang, F.; Li, Z.; et al. Tuning peptide self-assembly by an in-tether chiral center. *Sci. Adv.* **2018**, *4* (5), No. eaar5907.
(4) Lander, A. J.; Jin, Y.; Luk, L. Y. P. D-Peptide and D-Protein Technology: Recent Advances, Challenges, and Opportunities. *ChemBioChem.* **2023**, *24* (4), No. e202200537.
(5) Schumacher, T. N.; Mayr, L. M.; Minor, D. L., Jr; Milhollen, M. A.; Burgess, M. W.; Kim, P. S. Identification of D-peptide ligands through mirror-image phage display. *Science* **1996**, *271* (5257), 1854−1857.
(6) Zhou, M.; Wang, X.; Chen, B.; Xiang, S.; Rao, W.; Zhang, Z.; Liu, H.; Fang, J.; Yin, X.; Deng, P.; et al. Preclinical and first-in-human evaluation of $^{18}$F-labeled D-peptide antagonist for PD-L1 status imaging with PET. *Eur. J. Nucl. Med. Mol. Imaging* **2022**, *49* (13), 4312−4324.
(7) Hu, K.; Wu, W.; Xie, L.; Geng, H.; Zhang, Y.; Hanyu, M.; Zhang, L.; Liu, Y.; Nagatsu, K.; Suzuki, H.; et al. Whole-body PET tracking of a d-dodecapeptide and its radiotheranostic potential for PD-L1 overexpressing tumors. *Acta Pharm. Sin. B* **2022**, *12* (3), 1363−1376.
(8) Chang, H.; Liu, B.; Qi, Y.; Zhou, Y.; Chen, Y.; Pan, K.; Li, W.; Zhou, X.; Ma, W.; Fu, C.; et al. Blocking of the PD-1/PD-L1 Interaction by a D-Peptide Antagonist for Cancer Immunotherapy. *Angew. Chem.-Int. Ed.* **2015**, *54* (40), 11760−11764.
(9) Wang, L.; Zhang, H.; Huang, W.; Han, Z.; Xu, H.; Gu, Y. Development of a novel EphA2-targeting radioligand for SPECT imaging in different tumor models. *European Journal of Medicinal Chemistry* **2024**, *265*, 116105.
(10) Gao, X.; Xu, H.; Ye, Z.; Chen, X.; Wang, X.; Chang, Q.; Gu, Y. PDGFR$\beta$ targeted innovative imaging probe for pancreatic adenocarcinoma detection. *Talanta* **2023**, *255*, 124225.
(11) Yin, X.; Wang, X.; Chen, X.; Huang, K.; Han, Z.; Xu, H.; Gu, Y. A novel CXCR4-targeted peptide for SPECT/CT imaging in tumor. *Sensors and Actuators B: Chemical* **2024**, *410*, 135595.
(12) Li, J.; Wang, Q.; Xia, G.; Adilijiang, N.; Li, Y.; Hou, Z.; Fan, Z.; Li, J. Recent Advances in Targeted Drug Delivery Strategy for Enhancing Oncotherapy. *Pharmaceutics* **2023**, *15* (9), 2233.
(13) Cui, X.; Li, Z.; Kong, Z.; Liu, Y.; Meng, H.; Wen, Z.; Wang, C.; Chen, J.; Xu, M.; Li, Y.; et al. Covalent targeted radioligands potentiate radionuclide therapy. *Nature* **2024**, *630* (8015), 206−213.
(14) Li, X.; Lovell, J. F.; Yoon, J.; Chen, X. Clinical development and potential of photothermal and photodynamic therapies for cancer. *Nat. Rev. Clin. Oncol.* **2020**, *17* (11), 657−674.
(15) Zhang, L.; Zhang, S.; Wu, J.; Wang, Y.; Wu, Y.; Sun, X.; Wang, X.; Shen, J.; Xie, L.; Zhang, Y.; et al. Linear Peptide-Based PET Tracers for Imaging PD-L1 in Tumors. *Mol. Pharmaceutics* **2023**, *20* (8), 4256−4267.
(16) Pang, Y.; Zhao, L.; Fang, J.; Chen, J.; Meng, L.; Sun, L.; Wu, H.; Guo, Z.; Lin, Q.; Chen, H. Development of FAPI Tetramers to Improve Tumor Uptake and Efficacy of FAPI Radioligand Therapy. *J. Nucl. Med.* **2023**, *64* (9), 1449−1455.
(17) Liu, K.; Jiang, T.; Rao, W.; Chen, B.; Yin, X.; Xu, P.; Hu, S. Peptidic heterodimer-based radiotracer targeting fibroblast activation protein and integrin $\alpha_v\beta_3$. *Eur. J. Nucl. Med. Mol. Imaging* **2024**, *51* (6), 1544−1557.
(18) Quigley, N. G.; Tomassi, S.; di Leva, F. S.; Di Maro, S.; Richter, F.; Steiger, K.; Kossatz, S.; Marinelli, L.; Notni, J. Click-Chemistry (CuAAC) Trimerization of an $\alpha_v\beta_6$ Integrin Targeting Ga-68-Peptide: Enhanced Contrast for in-Vivo PET Imaging of Human Lung Adenocarcinoma Xenografts. *ChemBioChem.* **2020**, *21* (19), 2836−2843.
(19) Zhu, Z.; Miao, W.; Li, Q.; Dai, H.; Ma, Q.; Wang, F.; Yang, A.; Jia, B.; Jing, X.; Liu, S.; et al. $^{99m}$Tc-3PRGD2 for Integrin Receptor Imaging of Lung Cancer: A Multicenter Study. *J. Nucl. Med.* **2012**, *53* (5), 716−722.
(20) Bohnke, N.; Indrevoll, B.; Hammer, S.; Papple, A.; Kristian, A.; Briem, H.; Celik, A.; Mumberg, D.; Cuthbertson, A.; Zitzmann-Kolbe, S. Mono- and multimeric PSMA-targeting small molecule-thorium-227 conjugates for optimized efficacy and biodistribution in preclinical models. *Eur. J. Nucl. Med. Mol. Imaging* **2024**, *51* (3), 669−680.
(21) Zhang, H.; Koumna, S.; Pouliot, F.; Beauregard, J.-M.; Kolinsky, M. PSMA Theranostics: Current Landscape and Future Outlook. *Cancers* **2021**, *13* (16), 4023.
(22) Kunos, C. A.; Mankoff, D. A.; Schultz, M. K.; Graves, S. A.; Pryma, D. A. Radiopharmaceutical Chemistry and Drug Development—What's Changed? *Semin. Radiat. Oncol.* **2021**, *31* (1), 3−11.
(23) Luining, W. I.; Cysouw, M. C. F.; Meijer, D.; Hendrikse, N. H.; Boellaard, R.; Vis, A. N.; Oprea-Lager, D. E. Targeting PSMA Revolutionizes the Role of Nuclear Medicine in Diagnosis and Treatment of Prostate Cancer. *Cancers* **2022**, *14* (5), 1169.
(24) Kunos, C. A.; Martin, M. E.; Georgiou, M. F.; Kuker, R. A.; Chauhan, A. Leveraging Programmatic Collaboration for a Radiopharmaceutical Clinic. *Cancers* **2024**, *16* (7), 1396.
(25) Kunos, C. A.; Rubinstein, L. V.; Capala, J.; McDonald, M. A. Phase 0 Radiopharmaceutical-Agent Clinical Development. *Front. Oncol.* **2020**, *10*, 1310.
(26) Gomes Marin, J. F.; Nunes, R. F.; Coutinho, A. M.; Zaniboni, E. C.; Costa, L. B.; Barbosa, F. G.; Queiroz, M. A.; Cerri, G. G.; Buchpiguel, C. A. Theranostics in Nuclear Medicine: Emerging and Re-emerging Integrated Imaging and Therapies in the Era of Precision Oncology. *RadioGraphics* **2020**, *40* (6), 1715−1740.
(27) Hu, K.; Xie, L.; Zhang, Y.; Hanyu, M.; Yang, Z.; Nagatsu, K.; Suzuki, H.; Ouyang, J.; Ji, X.; Wei, J.; et al. Marriage of black phosphorus and $Cu^{2+}$ as effective photothermal agents for PET-guided combination cancer therapy. *Nat. Commun.* **2020**, *11* (1), 2778.
(28) Ayalew, B. D; Rodoshi, Z. N.; Patel, V. K; Alresheq, A.; Babu, H. M; Aurangzeb, R. F.; Aurangzeb, R. I.; Mdivnishvili, M.; Rehman, A.; Shehryar, A.; Hassan, A. Nuclear Cardiology in the Era of Precision Medicine: Tailoring Treatment to the Individual Patient. *Cureus* **2024**, *16* (4), No. e58960.
(29) Peştean, C.; Pavel, A.; Piciu, D. The Role of SPECT/CT and PET/CT Hybrid Imaging in the Management of Ectopic Thyroid Carcinoma—A Systematic Review. *Diagnostics* **2024**, *14* (13), 1369.
(30) Rimmerman, E. T.; Stacy, M. R. Applications of SPECT and PET Imaging for the Physiological Evaluation of Lower Extremity Peripheral Artery Disease. *Int. J. Mol. Sci.* **2024**, *25* (13), 7474.
(31) Sun, X.; Wu, Y.; Wang, X.; Gao, X.; Zhang, S.; Sun, Z.; Liu, R.; Hu, K. Beyond Small Molecules: Antibodies and Peptides for Fibroblast Activation Protein Targeting Radiopharmaceuticals. *Pharmaceutics* **2024**, *16* (3), 345.
(32) Wu, Y.; Sun, X.; Zhang, B.; Zhang, S.; Wang, X.; Sun, Z.; Liu, R.; Zhang, M.; Hu, K. Marriage of radiotracers and total-body PET/CT rapid imaging system: current status and clinical advances. *Am. J. Nucl. Med. Mol. Imaging* **2023**, *13* (5), 195−207.
(33) Qian, K.; Gao, S.; Jiang, Z.; Ding, Q.; Cheng, Z. Recent advances in mitochondria-targeting theranostic agents. *Exploration* **2024**, *4*, 20230063.


https://doi.org/10.1021/cbmi.4c00071
*Chem. Biomed. Imaging* 2025, 3, 180−190

(34) Xie, L.; Zhang, L.; Hu, K.; Hanyu, M.; Zhang, Y.; Fujinaga, M.; Minegishi, K.; Ohkubo, T.; Nagatsu, K.; Jiang, C.; et al. A $^{211}$At-labelled mGluR1 inhibitor induces cancer senescence to elicit long-lasting anti-tumor efficacy. *Cell Rep. Med.* **2023**, *4* (4), 100960.
(35) Baranyai, Z.; Reich, D.; Vágner, A.; Weineisen, M.; Tóth, I.; Wester, H.-J.; Notni, J. A shortcut to high-affinity Ga-68 and Cu-64 radiopharmaceuticals: one-pot click chemistry trimerisation on the TRAP platform. *Dalton Trans.* **2015**, *44* (24), 11137−11146.
(36) Asano, R.; Koyama, N.; Hagiwara, Y.; Masakari, Y.; Orimo, R.; Arai, K.; Ogata, H.; Furumoto, S.; Umetsu, M.; Kumagai, I. Anti-EGFR scFv tetramer (tetrabody) with a stable monodisperse structure, strong anticancer effect, and a long in vivo half-life. *FEBS Open Bio* **2016**, *6* (6), 594−602.
(37) Wu, J.; Zhao, C.; Lin, W.; Hu, R.; Wang, Q.; Chen, H.; Li, L.; Chen, S.; Zheng, J. Binding characteristics between polyethylene glycol (PEG) and proteins in aqueous solution. *J. Mater. Chem. B* **2014**, *2* (20), 2983−3150.
(38) Lai, J.; Yan, H.; Liu, Y.; Huang, Y. Effects of PEG molecular weight on its interaction with albumin. *Chin. J. Polym. Sci.* **2015**, *33* (10), 1373−1379.
(39) Chen, X.; Tohme, M.; Park, R.; Hou, Y.; Bading, J. R.; Conti, P. S. Micro-PET Imaging of $\alpha_v\beta_3$-Integrin Expression with $^{18}$F-Labeled Dimeric RGD Peptide. *Mol. Imaging* **2004**, *3* (2), 15353500200404109.
(40) Liu, S.; Liu, H.; Jiang, H.; Xu, Y.; Zhang, H.; Cheng, Z. One-step radiosynthesis of $^{18}$F-AlF-NOTA-RGD$_2$ for tumor angiogenesis PET imaging. *Eur. J. Nucl. Med. Mol. Imaging* **2011**, *38* (9), 1732−1741.
(41) Poethko, T.; Schottelius, M.; Thumshirn, G.; Hersel, U.; Herz, M.; Henriksen, G.; Kessler, H.; Schwaiger, M.; Wester, H.-J. Two-Step Methodology for High-Yield Routine Radiohalogenation of Peptides: $^{18}$F-Labeled RGD and Octreotide Analogs. *J. Nucl. Med.* **2004**, *45* (5), 892.
(42) Quigley, N. G.; Richter, F.; Kossatz, S.; Notni, J. Complexity of $\alpha_v\beta_6$-integrin targeting RGD peptide trimers: emergence of non-specific binding by synergistic interaction. *RSC Med. Chem.* **2023**, *14* (12), 2564−2573.
(43) Wu, Z.; Li, Z.-B.; Cai, W.; He, L.; Chin, F. T.; Li, F.; Chen, X. $^{18}$F-labeled mini-PEG spacered RGD dimer ($^{18}$F-FPRGD2): synthesis and microPET imaging of $\alpha_v\beta_3$ integrin expression. *Eur. J. Nucl. Med. Mol. Imaging* **2007**, *34* (11), 1823−1831.
(44) Zhang, M.; Kang, F.; Xing, T.; Wang, J.; Ma, T.; Li, G.; Quan, Z.; Yang, W.; Chen, X.; Wang, J. First-in-human validation of enzymolysis clearance strategy for decreasing renal radioactivity using modified [$^{68}$Ga]Ga-HER2 Affibody. *Eur. J. Nucl. Med. Mol. Imaging* **2024**, *51* (6), 1713−1724.
(45) Stangl, S.; Nguyen, N. T.; Brosch-Lenz, J.; et al. Efficiency of succinylated gelatin and amino acid infusions for kidney uptake reduction of radiolabeled $\alpha v\beta 6$-integrin targeting peptides: considerations on clinical safety profiles. *Eur. J. Nucl. Med. Mol. Imaging* **2024**, *51*, 3191−3201.


https://doi.org/10.1021/cbmi.4c00071
*Chem. Biomed. Imaging* 2025, 3, 180−190